Influence of the gate bias stress on the stability of n-type organic field-effect transistors based on dicyanovinylene-dihydroindenofluorene semiconductors

S. Bebiche, P.A. Cisneros-Perez, T. Mohammed-Brahim, M. Harnois, J. Rault-Berthelot, Cyril Poriel, E. Jacques

Influence of the gate bias stress on the stability of n-type Organic Field-Effect Transistors based on Dicyanovinylenes-Dihydroindenofluorene semiconductors

S. Bebiche[1], P. A. Cisneros-Perez[2], T. Mohammed-Brahim[1], M. Harnois[1], J. Rault-Berthelot[2], C. Poriel*[2], E. Jacques*[1]

[1] Univ Rennes, CNRS, IETR-UMR 6164, F-35000 Rennes, France

[2] Univ Rennes, CNRS, ISCR-6226, F-35000 Rennes, France

Abstract

The electrical stabilities of n-type Organic Field-Effect transistors (OFETs) based on dihydroindeno[1,2-*b*]fluorene and dihydroindeno[2,1-*b*]fluorene derivatives have been studied. These OFETs incorporate epoxy based photoresist SU-8 as gate insulator. The comparison of the electrical stability through gate bias stress measurements as a function of voltage and temperature stress shows that the instabilities of these OFETs result from different phenomena. Different models have been used to analyse the device's instabilities and are discussed. As the two molecules only differs by their geometry and by their substitution, this works shows how slight structural modifications of the semiconductor molecular structure induce electrical instabilities of the corresponding OFETs arising from different features.

Keywords: n-type Organic Field-Effect Transistors, Electrical Instability, Gate Bias Stress, Insulator Charge Trapping, Leakage Current, Dicyanovinylene-Dihydroindenofluorene

Introduction

Organic Field-Effects Transistors (OFETs) have encountered a fantastic development in the last twenty years and appear as a very promising technology for the future of electronics.[1, 2] These devices can be separated in two types following the accumulation of hole or electron into the active channel corresponding to p-type (hole-conducting) or n-type (electron-conducting) OFETs respectively. Despite the fantastic recent progresses in the field of n-type OFETs,[2-7] the p-type OFETs[8, 9] still present better characteristics (such as higher field-effect mobilities). This is mainly due to the fact that historically, the design of p-type materials has received most of the attention. However, highly efficient n-channel OFETs associated to p-channel OFETs are required to make complementary organic field-effect transistor digital circuits such as logic gates. An important parameter in OFETs for practical applications is the electrical stability. The electrical stability of an OFET can be evaluated by gate bias stress analysis. In such conditions, it is known that the threshold voltage shifts and the drain current I_D decreases.[10] As exposed above, p-type materials have been more developed than n-type ones, it is then obvious to find in

literature more studies related to the electrical stability of p-type OFETs[11-16] than n-type ones.[17, 18] Determining the origins of this threshold shift has been the subject of many researches.[19-22] and has allowed to better understand the stability of OFETs.

The present work aims to report our investigations on the electrical stability of n-type OFETs using as active layer a new electron-poor material based on the association of a dihydroindeno[1,2-*b*]fluorene core and dicyanovinylene groups (molecule **1**). These OFETs use as gate insulator the epoxy based photoresist SU-8. This choice is mainly driven to our need to reach in the near future fully organic OFETs and to better understand the organic-organic interface, key feature in this technology. Thus, OFET characteristics using (**1**) as active layer have been compared to those of using a structurally related material, dihydroindeno[2,1-*b*]fluorene (molecule **2**), previously reported in literature.[18, 23] The comparison of the electrical stability of these OFETs through gate bias stress measurements as a function of voltage and temperature stress shows that the instabilities result from different phenomena, namely the density defect creation and the charge trapping. Different models have been used to analyse the device's instabilities and are discussed. As the two molecules only differ by the geometry (syn for **(2)** and anti for **(1)**) and by the presence in **(1)** of pentyl side chains, this work shows how slight structural modifications of the semiconductor molecular structure induce electrical instabilities of the corresponding OFETs arising from different features.

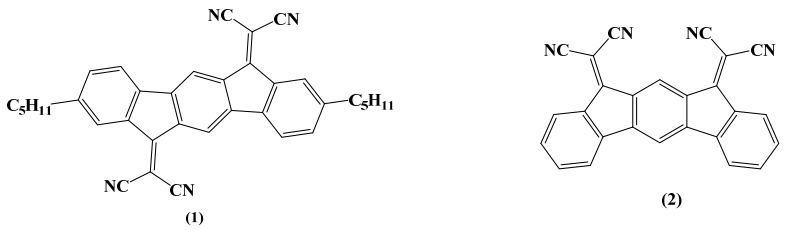

Fig. 1: Molecules investigated in this work based either on a dihydroindeno[1,2-*b*]fluorenyl core (**1**) or a dihydroindeno[2,1-*b*]fluorenyl core (**2**)

Chemistry

Dihydroindenofluorene positional isomers are a class of appealing organic semiconductors constituted of three bridged phenyl units, which have been widely studied in the last years.[24, 25] In the field of Organic Electronics, they have found promising applications as high triplet host materials in Phosphorescent Organic Light Emitting Diodes (PhOLEDs),[26-29] as blue emitters in OLEDs,[30-35] in solar cells[36, 37] and as n-type semiconductors in OFETs.[38-45] In this work, the new semiconductor **(1)** is constructed on the association of a 6,12-dihydroindeno[1,2-*b*]fluorene core, possessing on the bridges electron-withdrawing dicyanovinylene fragments. These fragments are known to strongly depress the LUMO energy level of the π-system bearing them.[46 17, 41, 46] In addition, pentyl side chains have been introduced on the C2 and C8 carbon atoms of the dihydroindeno[1,2-*b*]fluorene core. For comparison purpose, another dihydroindenofluorene positional isomer (5,7-dihydroindeno[2,1-*b*]fluorene) previously described in the

literature has also been investigated herein (molecule **(2)**).* [41] There are two structural differences between **(1)** and (**2**). The first is the geometry. Indeed, in **(2)**, the two dicyanovinylene units are on the same side of the dihydroindeno[2,1-*b*]fluorenyl backbone whereas in **(1)** they are on two opposite sides of the dihydroindeno[1,2-*b*]fluorenyl core. The second difference is the presence of pentyl side chains in **(1)**. These two parameters seem to have a crucial role in the performance and stability of the present OFETs investigated below.

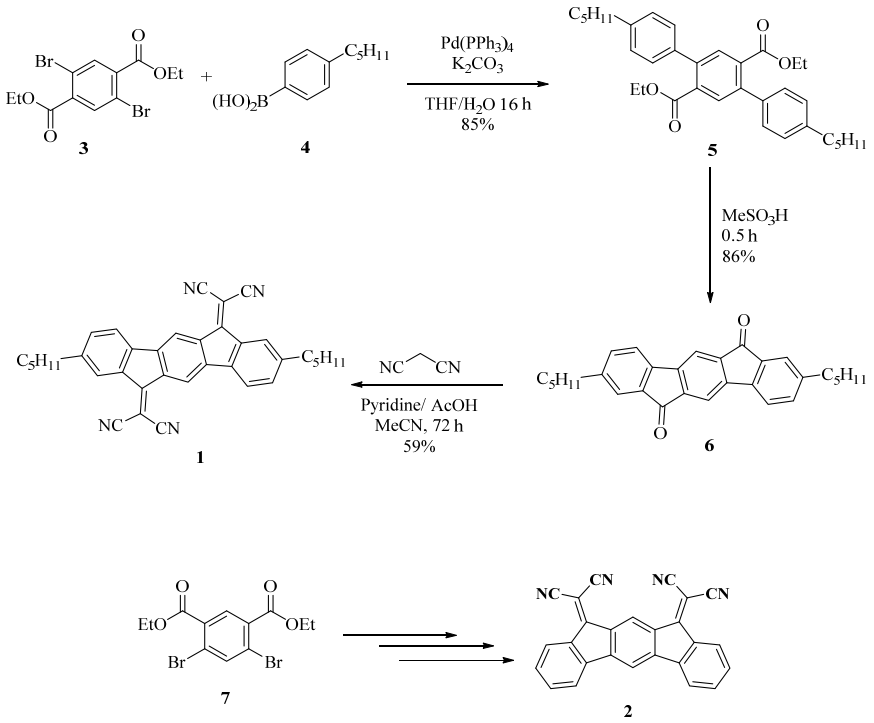

Scheme 1: Synthesis of **(1)** and **(2)**

The synthesis of **(1)** starts with the Suzuki-Miyaura cross coupling of dietyl 2,5-dibromoterephtalate **(3)** [47] with commercially available 4-pentylphenylboronic acid ($Pd(PPh_3)_4$, K_2CO_3, THF/H_2O) providing the corresponding terphenyl **(5)** with the ester groups on the central phenyl ring and in *ortho* position of one phenyl unit. Acid promoted ($MeSO_3H$) intramolecular Friedel-Crafts acylation[23, 48] of **(5)** at high temperature (120°C) readily took place to give the 2,8-dipentylindeno[1,2-*b*]fluorene-6,12-dione **(6)** with 86 % yield. It should be noted that **(6)** is soluble in common organic solvents and strongly more soluble than its non-substituted analogue indeno[1,2-*b*]fluorene-6,12-dione previously reported in literature.[49] With dione (**6**) in hand, a Knoevenagel condensation in the presence of malononitrile and pyridine was finally performed providing bisdicyanovinylene (**1**) with a good yield of 59% (see experimental part for synthetic details). One can note that this reaction does not use titanium tetrachloride, a Lewis acid frequently used to activate the carbonyl units in such a reaction.[46, 50] This route is easy to perform, efficient (overall yield of 43%) and allows a gram scale preparation of (**1**), which is a key feature for further devices applications. The synthesis of **(2)** is based on a similar strategy from diethyl 4,6-dibromoisophthalate **7** and has previously been reported.[41]

* Note that the corresponding 2,8-dipentyl-dihydroindeno[2,1-*b*]fluorene/dicyanovynilene has also been synthesized and studied in the course of this work. The electron mobility has been evaluated at $1.09\times10^{-4}cm^2/V.s$ but the corresponding OFET does not present stable transfer characteristics. This instability does not allowed to study these OFETs in detail (see SI for synthesis, properties and incorporation in OFETs of 2,8-dipentyl-dihydroindeno[2,1-*b*]fluorene/dicyanovynilene).

The determination of the LUMO energy level was of particular interest for the purpose of this work based on n-type OFETs as a low LUMO energy level is a key feature for charge injection within such device. The LUMO can be estimated by means of cyclic voltammetry as LUMO (eV)= -[E_{onset}^{red} (*vs* SCE) + 4.4] (based on an SCE energy level of 4.4 eV relative to the vacuum), Fig. 2.[51, 52] In dichloromethane, the voltamogramm of (**1**) displays two reversible waves with maxima recorded at -0.42 and -0.64 V vs SCE. Thus, the LUMO energy level of **(1)** has been estimated at ca -4.1 eV (E_{onset}=-0.30 V). This value appears to be very deep, highlighting the strong impact of the dicyanovinylene units on the dihydroindeno[1,2-*b*]fluorenyl core.[53] As the LUMO level of **(2)** has been reported at -3.81 eV, one can note that it is lowered by 0.30 eV compared to that of **(1)**. This difference can be assigned to structural deformations of the π-conjugated core of (**2**).[41]

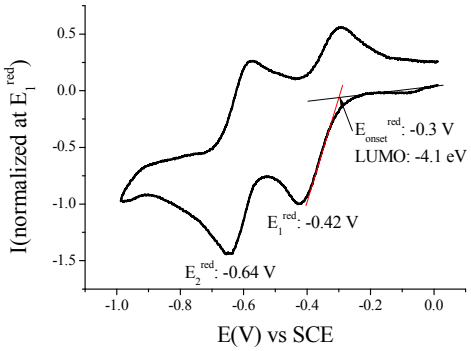

Fig. 2: Cyclic voltammetry at 0.1 V/s in CH_2Cl_2/[NBu_4][PF_6] 0.2 M in presence of **(1)**, platinum disk working electrode.

Organic Field-Effect Transistors

Compounds **(1)** and **(2)** were investigated through the fabrication and electrical characterization of bottom-gate bottom-contact n-type channel OFETs in which they were used as active layer (see OFET structure and fabrication process in the experimental part). SU8 photoresist used as insulator participates to the final goal to realize fully organic devices.[17] Moreover, as surface morphology of the gate dielectric affects the semiconductor layer growth, solution processed insulator remains the best way to ensure a smooth interface between these layers.

Transfer characteristics in linear (V_{DS}=10V) and saturation (V_{DS}=100V) regimes of **(1)** and **(2)** based OFETs are presented Fig. 3. The most important parameters, that is, the mobility μ_{FE}, the threshold voltage (V_{TH}), the subthreshold swing (SS), and the on/off values of the drain current I_D (I_{Don}/I_{Doff}) were extracted from the transfer characteristics in the linear and saturated regime and are gathered in Table 1.

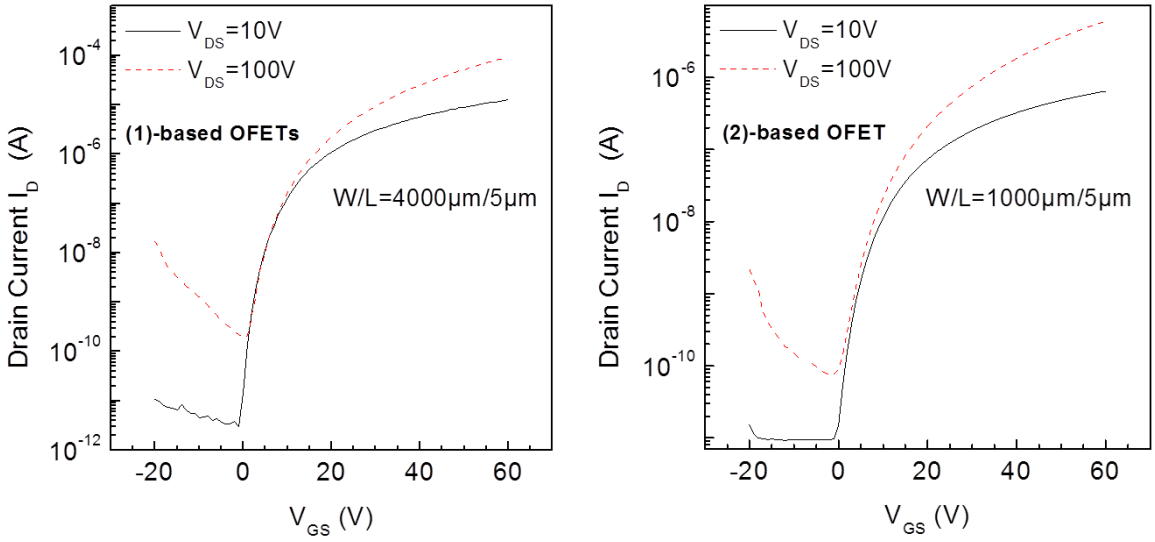

Fig. 3: Transfer characteristics in linear (V_{DS}=10V) and saturation (V_{DS}=100V) regimes of **(1)**-based OFETs (Left) and **(2)**-based OFETs (Right)

molecule	Regime	μ_{FE} (cm^2/V.s)	V_{TH} (V)	SS (V/dec)	I_{Don}/I_{Doff}
(1)	linear	0.005	26	1.3	4×10^6
	Saturation	0.021	20	1.9	5×10^5
(2)	linear	0.009	20	2.3	8×10^4
	Saturation	0.002	17	3.2	7×10^4

Table 1: Electrical characteristics of **(1)** and **(2)**-based OFETs

The threshold voltage values are similar for both OFETs, typically around 20V. This value can be nevertheless considered as high. However, it is clear that both OFETs can operate at lower voltage. Indeed, all previous parameters have been determined from the classical equations of MOSFETs (Metal Oxide Semiconductor Field-Effect Transistor), see experimental part, equations (1) to (4). Despite these equations are used for OFETs and more generally for disordered semiconductors based transistors, they were initially established for single crystalline silicon MOSFETs. However, in MOSFETs the swing off-on is very sharp with a subthreshold slope SS value below 100 mV/dec. For disordered material based FETs, the swing is very slow leading to operational transistors in the subthreshold regime. In other words, OFETs studied in this work could be polarized at values below the threshold voltage value.

The field-effect electron mobility of **(1)**-based OFETs in saturation was found to be 0.02 cm^2/V.s being 10 times higher than that of **(2)**-based OFETs, 0.002 cm^2/V.s. The value found for (**1**) appears to be

interesting for a dihydroindenofluorene but remain lower than those recently reported for indeno[1,2-*b*]fluorenones bearing either S-butyl side chains (0.65 $cm^2/V.s$) [42] or thiophene units (0.12 $cm^2/V.s$)[44] with nevertheless different device architectures. One can also note that the I_{Don}/I_{Doff} ratio is significantly higher for **(1)**-based OFETs compared to **(2)**-based OFETs both in linear and saturation regimes (Table 1). These I_{Don}/I_{Doff} values obtained for **(1)**-based OFETs (4×10^6) appear promising for practical applications. Finally, the SS value of **(1)**-based OFETs (1.3 V/dec in linear regime) is also appealing for circuits and appear again better than that of **(2)**-based OFETs (2.3 V/dec). The electrical quality of the insulator-semiconductor interface can be involved in the good SS value. All these features clearly highlight that switching from the *syn* geometry found in the previously reported dihydroindeno[2,1-*b*]fluorene core of **(2)** to an *anti* geometry in the present dihydroindeno[1,2-*b*]fluorene core of **(1)** coupled to the addition of pentyl side chains have beneficial effects on both the field-effect mobility, the I_{Don}/I_{Doff} ratio and the SS without negative consequences on V_{TH}.

It should be mentioned that the groups of Marks and Fachetti have reported a structurally related dicyanovinylenes-dihydroindeno[1,2-*b*]fluorene semiconductor possessing dodecanyl chains on the central phenyl ring. This compound did not possess any FET activity.[39] Thus, the shortening of the alkyl chains (from C12 to C5) and their shifts to the side phenyl rings has an impressive beneficial effect on the field-effect mobility.

It is important to stress that the present OFET structure (i) is nearly fully organic based with only the electrodes made in an inorganic material and (ii) has no particular treatment onto electrode surface or on gate insulator (before deposition of active layer). With device engineering (such as the grafting of self-assembled monolayers of 4-(dimethylamino) benzenethiol on the electrodes as previously reported on structurally related semiconductors),[17] we are convinced that present performance of (**1**)-based OFETs can be increased in future works.

Although the mobility, the subthreshold slope, the threshold voltage and the I_{Don}/I_{Doff} ratio provide interesting information to compare organic semiconductors in an OFET, they are not sufficient to perfectly understand their behaviour in a circuit. The behaviour of the active layer under polarization is hence crucial to further achieve a circuit and the electrical stability of OFETs is one of the central parameter for a practical use.

We first focus on the electrical behaviour of OFETs under a low ($V_{GSstress}-V_{TH}$=20 V, Fig. 4-Bottom) and a high ($V_{GSstress}-V_{TH}$=40 V, Fig. 4-Top) gate bias stress both being higher than threshold voltage. This experiment, called gate bias stress, consists to apply a high bias voltage on gate electrode to maintain the OFET in on-regime. The stress voltage is applied for a total duration of 3 hours. Drain and source electrodes are grounded in order to uniformly stress the channel. At regular intervals of time, the stress is removed and transfer characteristics are plotted.

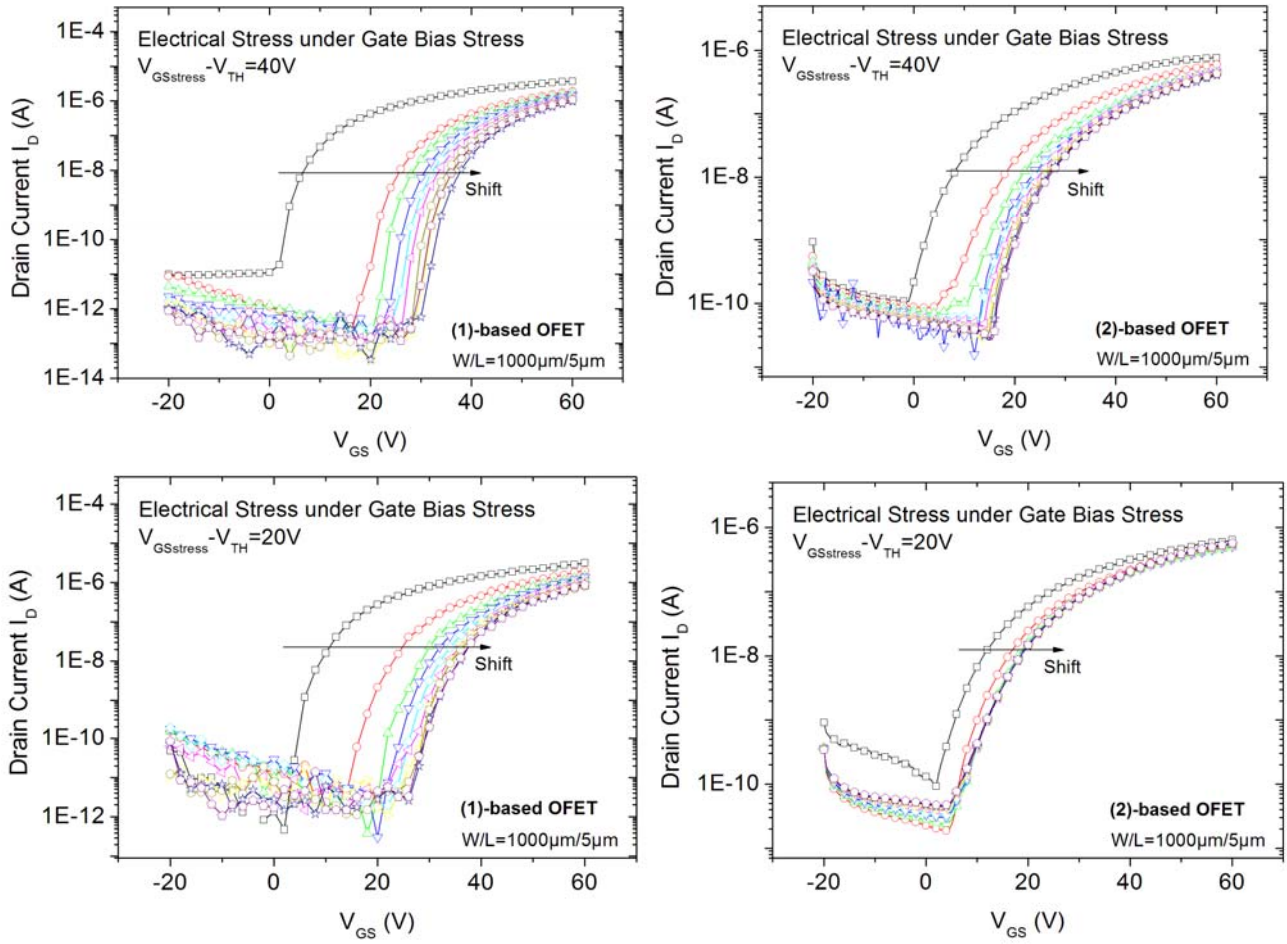

Fig. 4: Transfer characteristics of **(1)** and **(2)**-based OFETs recorded at different times (every 20 minutes) of gate bias stress for $V_{GSstress}$-V_{TH}=40V (Top) and for $V_{GSstress}$-V_{TH}=20V (Bottom).

For all experiments, we first note a significant shift of the threshold voltage (ΔV_{TH}) toward positive values (Fig. 4). This is a classical behaviour.[20] ΔV_{TH} reaches its highest value during the first 20 minutes of stress and then gradually decreases.

At $V_{GSstress}$-V_{TH}=40V, we note for both OFETs that the maximum current (at V_{GS}=60V) decreases with the stress time whereas the threshold voltage increases (Fig. 4). For **(2)**-based OFET, the maximum current decreases by 40% and the threshold voltage increases by 60%. Both variations are larger for **(1)**-based OFET. As the current decreases by 70% and the threshold voltage increases by 100%, from a molecular point of view, we hypothesize that the difference between the two molecules can be ascribed to the alkyl chains borne by **(1)**. However, these gate bias stress effects deserve to be discussed in detail, see below.
At $V_{GSstress}$-V_{TH}=20 V (Figure 4, bottom), the same conclusions than those above exposed for $V_{GSstress}$-V_{TH}=40 V can be drawn for both OFETs with nevertheless a striking difference. Indeed, ΔV_{TH} is strongly attenuate in the case of **2** whereas ΔV_{TH} remains almost identical in the case of **1**. Thus, we note a different V_{TH} shift as a function of the stress applied. This leads us to more precisely investigate this feature. Two different mathematical models (Equations 5 and 6) are used herein to understand these gate bias stress variations presented above: a stretched exponential law (Equation 5) which implies a defect density creation[54] within the organic semiconductor and a charge carrier trapping law (Equation 6) occurring inside the gate insulator.[55]

In case of a defect density creation, the V_{TH} variation with the stress time t is described by a stretched exponential law:

$$V_{TH}(t) - V_{TH}(0) = (V_{GSstress} - V_{TH}(0))\left\{1 - exp\left[-(t/t_0)^{\beta}\right]\right\} \qquad (5)$$

Where $V_{GSstress}$ is the gate voltage applied during the stress, $V_{TH}(0)$ is the initial threshold voltage, t_0 and β are fit parameters. β is related to width of the involved trap distribution and τ is related to trapping time.

The stretched exponential law is usually involved to describe relaxation phenomena in glasses towards equilibrium under different stresses.[56] This law was established considering a diffusion of specific particles in a material with a randomly distributed energy states. These states are able to trap these particles ('trapping sites').[57] In disordered materials, containing metastable states, some physical parameters such as conductivity,[58] threshold voltage of FETs [54] or magnetization[56] evolve following a stretched exponential law. In amorphous silicon TFTs, this effect has been associated to a dispersive diffusion coefficient of atomic hydrogen.[54] This dispersion comes from the nature of any disordered material in which the trapping sites present a distribution of energy states. The β parameter in equation 5 is related to this distribution of states and to the temperature. Most of the time, this law is efficient to describe the effect of any applied stress in a wide panel of situations. In single crystalline silicon based MOSFET[59] and polycrystalline silicon TFTs, the V_{TH} shift is related to the disordered gate insulator/active layer interface. In this case, the dispersive diffusion within gate insulator/active layer interface (disordered material) can be involved. In disordered materials in general, any energy absorption, inducing new charge carriers distribution, can change the state of the weakest bonds, then disturbing the equilibrium. The deformation can diffuse through the material leading to a new equilibrium state characterized by new defect distribution.

To explain the effect of the gate bias stress, another explanation involves a charge carrier trapping inside the gate insulator.[55] This carrier trapping can be negligible in most of OFETs which use inorganic silicon dioxide as gate insulator. However, as the present gate insulator is an organic material i.e. SU8 photoresist, the trapping model deserves to be precisely investigated. This model involves an injection of carriers inside the insulator due to the applied gate bias stress. These carriers are trapped inside the insulator fixing an electrical charge which creates an opposite electric field nearby the channel. Consequently, the effective gate voltage changes inducing the charge accumulation in the channel and leading to drain current variation. The threshold voltage variation is described by logarithmic stress time dependence. [55]

$$V_{TH}(t) - V_{TH}(0) = r_d \log\left(1 + \frac{t}{t_0}\right) \qquad (6)$$

This logarithmic evolution arises from the phenomenon of charges injection through tunnelling effects, where the injected current exponentially depends on the density of previously injected charges.[60] This means an exponential decrease of the injected current. r_d and t_0 are fit parameters with r_d is related to the trapped carriers density in the insulator and t_0 is related to trapping time.

In order to investigate which model can be used in the present case, two gate bias stress ($V_{GSstress}$-V_{TH}=20V or 40V) and two different temperatures (30 and 40°C) for both **(1)**- and **(2)**-based OFETs were investigated. The purpose is to favour the defect density creation and to evaluate the effect of the stress temperature.

We first started with a stress applied on the know compound **(2)** at a low stress voltage, $V_{GSstress}$-V_{TH}=20V and for 2 different temperatures, 30°C and 40°C (Fig. 5a). The threshold voltage behaviour of these OFETs during the stress was successfully fitted by the stretch exponential model, ie equation (5), describing the defect density creation (correlation factors are 0.995 and 0.991 at 30°C and 40°C respectively). The values obtained ($\beta = 0.18$ and $t_0=5.5\times10^3$ sec at 30°C and $\beta = 0.28$ and $t_0=2\times10^3$ sec at 40°C) appear to be similar to those reported in literature for amorphous silicon FETs[61] and as expected β increases and t_0 decreases with the temperature. The maximum V_{TH} shift increases with the temperature, which is a coherent feature since trapping is enhanced when higher density of carriers is generated in the channel. One can conclude that the stretch exponential model is suitable with the present stress and V_{TH} shift could be attributed to defect density creation in the active layer. However, fitting the same experimental curves with the equation 6 corresponding to the trapping model attenuate this assignment. Indeed, Fig. 5b shows the same experimental curves than those presented in Fig. 5a but fitted with the trapping law (equation 6). It is clear that both experimental curves at 30 and 40°C are also well fitted by this relation with r_D=3.82 and t_0=0.4s at 30°C and r_D=5.7 and t_0=3.3s at 40°C (correlation factors are 0.995 and 0.992 at 30°C and 40°C respectively).

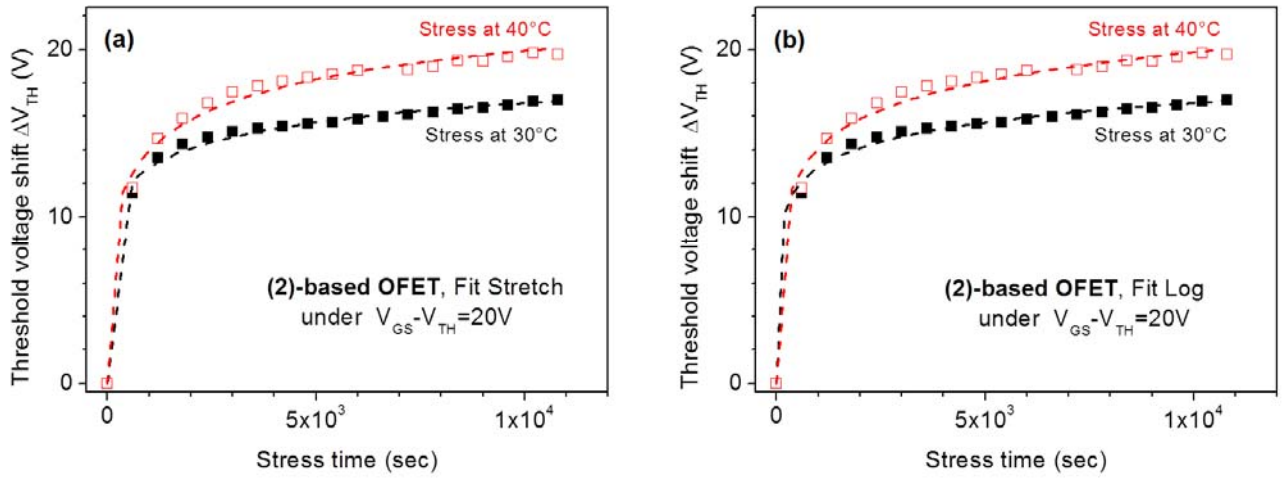

Fig. 5: Evolution of ΔV_{TH} with the stress time for **(2)**-based OFETs under $V_{GSstress}$-V_{TH}=20V at 30°C and 40°C. (a) The dashed lines are the fit with stretched exponential equation (5). (b) The dashed lines are the fit with logarithmic equation (6)

To conclude, both experimental curves were well fitted by both the equations 5 and 6, describing respectively the defect density creation inside the active layer and the carrier trapping at the gate insulator. The correlation coefficients are nearly the same. This fit alone does not allow discriminating between the two models and a possible explanation is that both phenomena simultaneously occur in the present stress conditions. This statement has also been observed when using different insulator layers to understand the dominant effect of threshold voltage shift.[62]

Interestingly, the investigations of **(1)**-based OFETs in identical experimental conditions ($V_{GSstress}$-V_{TH}=20V) provide very different results. Indeed, attempts to fit the V_{TH} shift with the stretched exponential law (equation 5) fails and on the contrary, the fit with trapping law (equation 6) succeeds (Fig. 6a). The correlation factor is 0.996 and the parameters r_d and t_0 are 10.7 and 28.8 sec respectively at T=30°C. One can hence conclude that the instability of **(1)**-based OFETs under low gate bias stress arises

from carrier trapping occurring inside the gate insulator. This is a different behaviour than that exposed above for (**2**).

In conclusion, under low gate bias stress (20 V), V_{TH} shift of **(2)**-based OFETs seems to be due to both the defect density creation inside the active layer and the carrier trapping inside the gate insulator. On the contrary, V_{TH} shift of **(1)**-based OFET seems to be entirely due to the carrier trapping in the insulator. This indicates not only a better stability of the semiconductor **(1)** under electrical stress but more importantly a very different trapping behaviour compared to its structurally analogue **(2)**. This observation could be argued by a higher gate leakage current in (**1**)-based OFETs (Fig. 6b) compared to (**2**)-based OFETs increasing the probability to trap charges into the insulator. From a molecular point of view, switching from a syn geometry in **2** to an anti geometry in **1** and introducing in the meantime pentyl side chains has significantly changed the origin of the OFETs electrical instabilities. The origins of these electrical instabilities come from a different insulator/semi-conductor interface. This work shows how slight structural modifications of the molecular structure of the semiconductor can lead to different insulator/semi-conductor interfaces and hence to electrical instabilities arising from different features. Interface effects on the electrical instabilities have previously been approached by Ahmed *et al.*[63, 64]

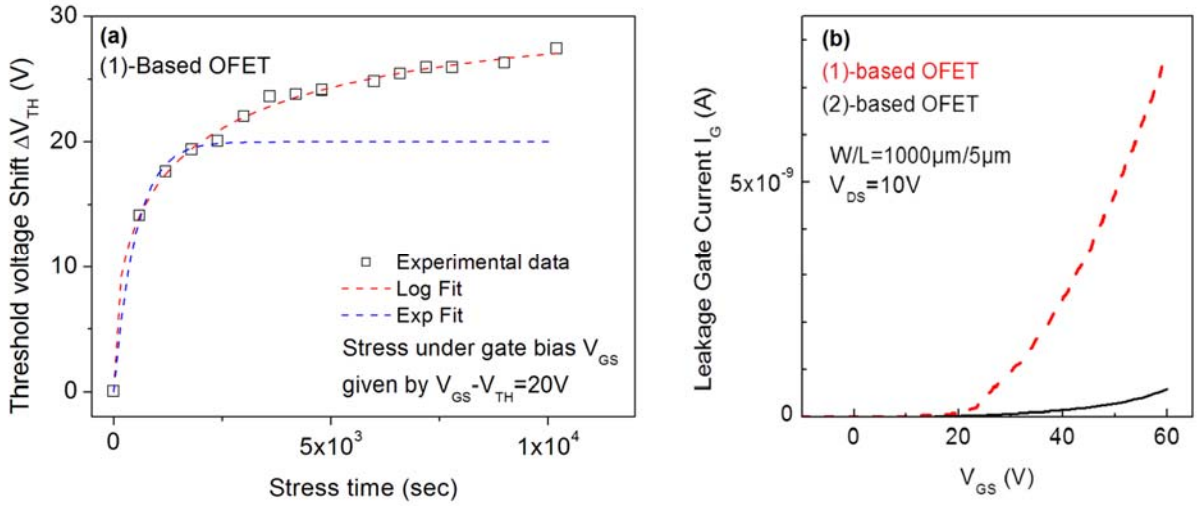

Fig. 6: (a) V_{TH} shift with the stress time under $V_{GSstress}$-V_{TH}=20V for **(1)**-based OFETs. Red dashed lines correspond to fit with logarithmic equation 6 and blue dashed lines correspond to fit with stretched-exponential equation 5. (b) Gate leakage current in (**1**) and (**2**)-based OFET

In a second step, similar studies were performed by increasing the gate bias stress ($V_{GSstress}$-V_{TH}=40V) of **(1)** and **(2)**-based OFETs. The goal was to investigate the influence of the gate bias stress on the origin of the instabilities. This should lead to prominent trapping as tunnelling phenomena such as Fowler-Nordheim tunnelling generally occur at high applied voltage.[57] For both **(1)** and **(2)**-based OFETs, the experimental curves are well fitted (Fig. 7a) exclusively by equation 6 and not by equation 5. One can hence conclude that at high stress voltage, the V_{TH} shift of both **(1)** and **(2)**-based OFETs follow the same trapping law.

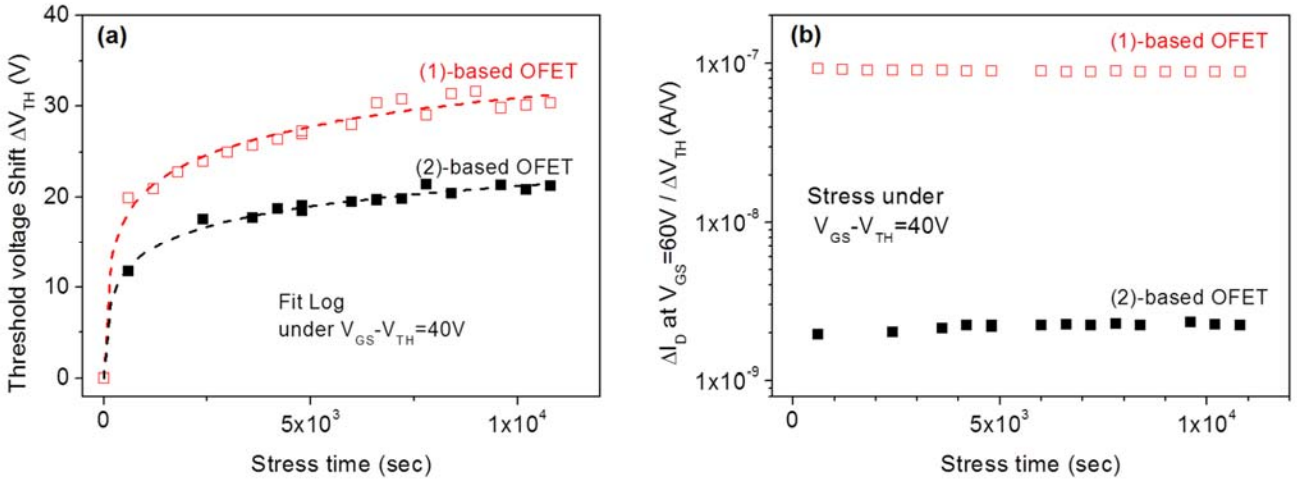

Fig. 7: (a) V_{TH} shift with the stress time for **(1)** and **(2)**-based OFETs under $V_{GSstress}$-V_{TH}=40V. The dashed lines correspond to fit with logarithmic equation (6). (b) $\frac{\Delta I_D}{\Delta V_{TH}}$ ratio as a function of stress time for **(1)** and **(2)**-based OFETs under $V_{GSstress}$-V_{TH}=40V

In order to highlight this phenomenon, the ratio between the current variation and the V_{TH} shift is plotted in Fig. 7b as a function of the stress time for both OFETs. At constant V_{GS}, fixed at 60V, and constant V_{DS}, fixed at 10V, the ratio current variation on threshold voltage shift is given by:

$$\frac{\Delta I_D}{\Delta V_{TH}} = -\frac{W}{L}\mu_{FE}C_{insulator}V_{DS} \qquad (7)$$

Importantly, we note for both OFETs that the ratio remains constant during the stress. This constant ratio means constant field-effect mobility during the stress. Consequently, the transport properties in the active layer do not change during the stress ruling out the defect density creation inside the active layer for both **(1)**- and **(2)**-based OFETs under high gate bias stress and confirming therefore the carrier trapping within the insulator.

Finally, the V_{TH} shift difference between **(1)** and **(2)**-based OFETs should be explained. Indeed, as above mentioned, the V_{TH} increases by 100% for **(1)**-based OFETs and only by 60% for **(2)**-based OFETs after 3 hours of $V_{GSstress}$-V_{TH}= 40V stress (Fig. 4). To explain the difference, the phenomenon of charge injection through tunnelling effects responsible of the carrier trapping can be involved. Here, the injected current is the leakage gate current I_G in the gate insulator. The variation of the trapped charges ΔQ is proportional to the injected current in the insulator. Due to the screening of previously trapped charges, the injected current decreases during the stress. The variation of these trapped charges is found to be

responsible of V_{TH} shift ($\Delta V_{TH}=-\Delta Q/C_{insulator}$). With this explanation, the gate leakage current is expected to decrease during the gate bias stress. In this case, its decrease is expected to be proportional to V_{TH} shift. Fig. 8 shows the decrease of the gate leakage current with the stress time for **(1)**-based OFETs. Plotting I_G current as a function of V_{TH} shift confirms the linear dependence between these two parameters (Fig. 8b). Therefore, Fig. 8 confirms that the effect of gate bias stress on **(1)**-based OFETs is due to carrier trapping inside the gate insulator. More generally, we can expect a significant V_{TH} shift depending on the initial value of the gate current in the case where carrier trapping phenomenon is involved. Thus, the larger V_{TH} shift observed for **(1)**-based OFETs compared to **(2)**-based OFETs, under the same gate bias stress, could be explained by the higher gate leakage current initially observed in the device (Fig. 6b).

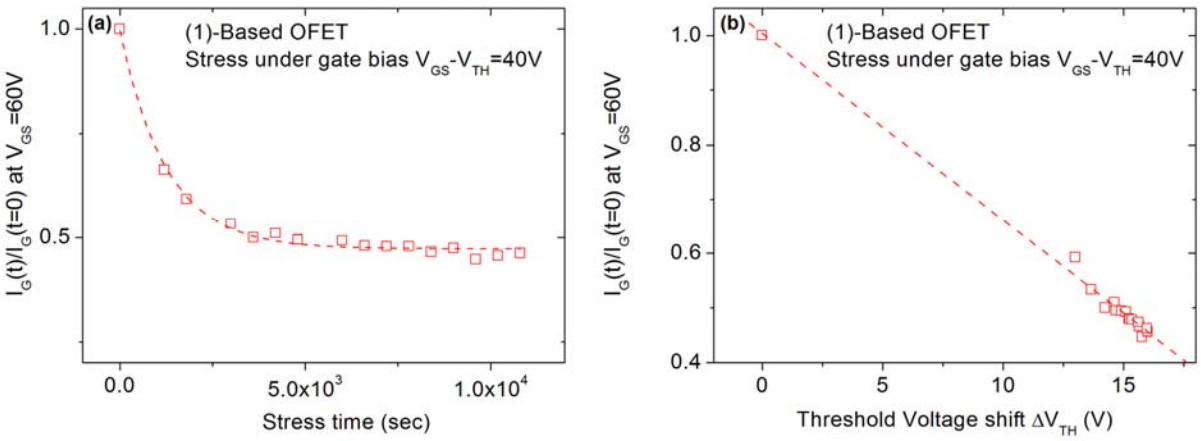

Fig. 8: (a) Decrease of leakage current I_{GS} (at V_{GS}=60V) for **(1)**-based OFETs during stress time under $V_{GSstress}$-V_{TH}=40V. (b) Linear relationship between I_G and V_{TH} for **(1)**-based OFETs under $V_{GSstress}$-V_{TH}=40V

Conclusion

In this work, we report our investigations on the electrical stability of n-type OFETs based on electron-poor dihydroindenofluorene derivatives incorporating dicyanovinylene fragments. First, we have shown that the new dihydro[1,2-*b*]indenofluorene semiconductor **1** present better OFETs characteristics than those of the previously reported dihydro[2,1-*b*]indenofluorene semiconductor **2** (higher μ_{FE} and I_{Don}/I_{Doff}, lower SS). However, despite better electrical parameters, molecule **1** leads to less stable OFETs than molecule **2**, showing that the most efficient device is not always the most stable one. This is an important feature for practical applications of OFETs.

More importantly, we have surprisingly shown that the threshold voltage shift of the OFETs based on these two structurally related molecules arise from different features. Indeed, at low gate bias stress, the carrier trapping inside the insulator well explains the instability of **(1)**-based OFETs whereas for **(2)**-based OFETs, both the carriers trapping inside the insulator and the defect density creation inside the active layer can be involved. At high gate bias stress, the situation is again different as only the carriers trapping inside the insulator is involved for both **(1)** and **(2)**-based OFETs.

In addition, this work has also shown that **(1)**-based OFET displays a larger V_{TH} shift than **(2)**-based OFET (under the same gate bias stress), which has been assigned to a higher gate leakage current in the former. This feature can be related to the different insulator/semi-conductor interfaces. Thus, this work shows how slight structural modifications of the molecular structure of the semiconductor can induce electrical instabilities of the corresponding OFETs arising from different features.

Acknowledgment
This work is supported by the European Union through the European Regional Development Fund (ERDF), the Ministry of Higher Education and Research, the Région Bretagne, the Département d'Ille et Vilaine and Rennes Metropole, through the CPER Project 2015-2020 MATECOM-ORGAFLEX. The authors wish to thank the C.R.M.P.O (Rennes) for mass analysis. CP wishes to thank the UMR CNRS 6226-Institut des Sciences Chimiques de Rennes for an 'Inter UMR' grant, Dr Maxime Romain for his help and Prof B. Frontana Uribe (UNAM Mexico). EJ wishes to thanks the IETR for financial support.

Experimental Part.

Synthesis:

All manipulations of oxygen- and moisture-sensitive materials were conducted with a standard Schlenk technique. Commercially available reagents and solvents were used without further purification other than those detailed below. THF was distilled from sodium/benzophenone prior to use. Light petroleum refers to the fraction with bp 40-60°C. Reactions were stirred magnetically, unless otherwise indicated. Analytical thin layer chromatography was carried out using aluminium backed plates coated with Merck Kieselgel 60 GF254 and visualized under UV light (at 254 and 360 nm). Chromatography was carried out using Teledyne Isco CombiFlash® Rf 400 (UV detection 200-360 nm), over standard silica cartridges (Redisep® Isco). ^{1}H and ^{13}C NMR spectra were recorded using Bruker 300 MHz instruments (^{1}H frequency, corresponding ^{13}C frequency: 75 MHz); chemical shifts were recorded in ppm and J values in Hz. In the ^{13}C NMR spectra, signals corresponding to C, CH, CH_2 or Me groups, assigned from DEPT, are noted. The residual signals for the NMR solvents are: $CDCl_3$; 7.26 ppm for the proton and 77.00 ppm for the carbon. The following abbreviations have been used for the NMR assignment: s for singlet, d for doublet, t for triplet and m for multiplet.
2 has been synthesized according to literature procedures with spectroscopic analyses and purity in accordance with those of our previous works.[41] The optical and electrochemical properties of **2** can be found in our previous works.[41]

1 has been synthesized as presented below.
Diethyl 4,4''-dipentyl-[1,1':4',1''-terphenyl]-2',5'-dicarboxylate (5):
Diethyl 2,5-dibromoterephthalate **3** (0.390 g, 1.0 mmol), 4-pentylphenylboronic acid **4** (0.500 g, 2.5 mmol), tetrakis(triphenylphosphine) palladium^{0} (0.115 g, 0.10 mmol) and potassium carbonate (0.700 g, 5 mmol) were dissolved in a THF/water mixture (2.5:1, 35 ml) under an argon atmosphere. The resulting mixture was degassed and stirred 16 h at 75°C. The resulting mixture was quenched with a saturated solution of ammonium chloride (20 ml) and extracted with ethyl acetate (2×50 ml). The combined extracts were dried over $MgSO_4$, filtered, evaporated *in vacuo* and purified by column chromatography on silica gel eluting with a gradient of light petroleum-ethyl acetate (100:0 to 95:5) to give the *title compound* as a colorless solid (0.437 g, 85%). mp 92-94 ˚C (from ethyl acetate) ν_{max} /cm^{-1} 2956, 2942, 2873, 2837, 1714 (CO), 1463, 1274, 1112, 848, 590; ^{1}H NMR (300 MHZ; $CDCl_3$) δ 7.80 (2H, s, Ar-H), 7.30-7.27 (4H, d, *J* 8.1, Ar-H), 7.24-7.21 (4H, d, *J* 8.1, Ar-H), 4.16-4.08 (4H, q, J 7.5, OCH_2Me), 2.68-2.63 (4H, t, *J* 7.5, Ar-CH_2CH_2), 1.69-1.64(4H, m, *J* 7.5, Ar-CH_2CH_2), 1.38-1.35(8H, m, CH_2), 1.04-0.99 (6H, t, *J* 7.5, OCH_2Me), 0.94-0.89 (6H, t, *J* 7.5, CH_2Me); ^{13}C NMR (75 MHz, $CDCl_3$) δ 168.3 (CO), 142.4 (C), 140.8 (C), 137.4 (C), 133.5 (CH), 131.7 (CH), 128.3 (CH), 128.2 (CH), 61.2 (CH_2), 35.6 (CH_2), 31.5 (CH_2), 31.1 (CH_2), 22.5 (CH_2), 14.0 (CH_3), 13.7 (CH_3).

2,8-dipentylindeno[1,2-*b*]fluorene-6,12-dione (6):
Diethyl 4,4''-dipentyl-[1,1':4',1''-terphenyl]-2',5'-dicarboxylate **5** (0.41 g, 0.8 mmol) was dissolved in methane sulfonic acid (8 ml) and stirred 30 minutes at 120 °C. The solution was then poured into 10 % aqueous sodium hydroxide to pH=14. The precipitate formed was collected by filtration, washed with 150 ml water, dissolved in 200 ml of dichloromethane, re-filtered over a pad of silica gel (4 cm), the solvent was removed *in vacuo*. The *title compound* was obtained as a red solid (0.302 g, 86%); mp 198-200 ˚C (from dicholoromethane) ν_{max} /cm^{-1} 2960, 2939, 2899, 1706 (CO), 1610, 1452, 1213, 1140, 838, 777, 520; ^{1}H NMR (300 MHZ; $CDCl_3$) δ 7.62 (2H, s, Ar-H), 7.43 (2H, s, Ar-H), 7.38-7.35 (2H, d, *J* 7.8, Ar-H), 7.30-7.28 (2H, dd, *J* 7.5, 1.5, Ar-H), 2.62-2.57 (4H, t, *J* 7.5, Ar-CH_2CH_2), 1.66-1.56 (4H, m, *J* 7.5, Ar-CH$_2$CH_2), 1.34-1.24 (8H, m, CH_2), 0.92-0.87 (6H, t, *J* 7.5, CH$_2$Me); ^{13}C NMR (75 MHz, $CDCl_3$) δ 192.5 (CO), 144.9 (C), 144.1 (C), 140.45 (C) , 138.6 (C), 134.5 (C), 133.5 (CH), 123.7 (CH), 119.6 (CH), 114.8 (CH), 35.0 (CH_2), 30.6 (CH_2), 30.0 (CH_2), 21.7 (CH_2), 13.2 (CH_3). UV-vis (CH_2Cl_2) [λ max/nm (ε in L mol^{-1} cm^{-1})] = 295 (1.48×10^5), 285.5 (17.4×10^4), 269 (3.0×10^4)

2,2'-(2,8-dipentylindeno[1,2-*b*]fluorene-6,12-diylidene)dimalononitrile (1)
2,8-dipentylindeno[1,2-b]fluorene-6,12-dione **6** (0.360 g, 0.8 mmol) and malononitrile (1.056 g, 16 mmol) were dissolved in dry acetonitrile (35 ml) under argon atmosphere. Pyridine (1.61 ml, 20 mmol) and acetic acid (0.56 ml, 10 mmol) were added via syringe. The resulting mixture was stirred 72 hours at reflux. Upon cooling, water (50 mL) was added and the red precipate formed was filtered off, washed several times with water and acetone. The filtrate was suspended in 20 ml of dichloromethane and stirred for 20 min. The suspension was filtered and the precipitate was dried in an oven at 80 ˚C overnight. (0.244 g, 59%); mp 320-322 ˚C (from dicholoromethane) ν_{max} /cm^{-1} 2962, 2929, 2889, 2227(CN), 1576, 1492, 1448, 1377, 895, 842, 740, 596; ^{1}H NMR (300 MHZ; $CDCl_3$) δ 8.44 (2H, s, Ar-H), 8.16 (2H, s, Ar-H), 7.53-7.50 (2H, d, *J* 7.8, Ar-H), 7.37-7.34 (2H, dd, *J* 7.5, 1.5, Ar-H), 2.68-2.62 (4H, t, *J* 7.5, Ar-CH_2CH_2), 1.65-1.60 (4H, m, Ar-CH$_2$CH_2), 1.34-1.30 (8H, m, CH_2), 0.89-0.85 (6H, t, *J* 7.5, CH$_2$Me). UV-vis (CH_2Cl_2) [λ max/nm (ε in L mol^{-1} cm^{-1})]= 403 (1.85×10^4), 382.5 (1.90×10^4), 319 (5.4×10^4), 305.5 (8×10^4)

Electrochemical studies:

Electrochemical experiments were performed under an argon atmosphere, using a Pt disk electrode (diameter 1 mm), the counter electrode was a vitreous carbon rod and the reference electrode was a silver wire in a 0.1 M $AgNO_3$ solution in CH_3CN. Ferrocene was added to the electrolytic solution at the end of a series of experiments. The ferrocene/ferrocenium (Fc/Fc^+) couple served as internal standard. The three electrode cell was connected to a PAR Model 273 potentiostat/galvanostat (PAR, EG&G, USA) monitored with the ECHEM Software. Activated Al_2O_3 was added in the electrolytic solution to remove excess moisture. All potentials are referred to the SCE electrode that was calibrated at 0.405 V *vs*. Fc/Fc^+ system. Following the work of Jenekhe, we estimated the electron affinity (EA) or lowest unoccupied molecular orbital (LUMO) from the redox data. The LUMO level was calculated from: LUMO (eV)= -[E_{onset}^{red} (*vs* SCE) + 4.4] based on an SCE energy level of 4.4 eV relative to the vacuum.[51, 52]

OFETs Fabrication and Characterization

Bottom gate-bottom contacts transistors were fabricated on glass substrates. Substrates were previously cleaned with acetone and rinsed with ethanol. An aluminium layer of 150 nm is then deposited by thermal evaporation and wet etched to define gate electrodes. 320 nm thick SU-8 photoresist (from Microchem) was spin-coated and then exposed to UV light to define gate insulating layer (see MicroChem Su-8 2000

Permanent Epoxy Negative Photoresist Processing Guidelines for Su-8 2000.5, Su-8 2002, So-8 2005, Su-8 2007, Su-8 2010 and Su-8 2015-http://www.microchem.com/pdf/SU-82000DataSheet2000_5thru2015Ver4.pdf). Then, 60 nm thick gold film was thermally evaporated and then wet etched to form source and drain electrodes. Finally, the active layer was deposited by thermal evaporation under a high vacuum of 3.10^{-7} mbar. Substrate temperature was kept constant (T_{sub}=30°C), deposition rate and layer thickness were fixed to 0.4 Å/s and 8 nm respectively. After fabrication, a post annealing treatment on both devices at 110°C during 90 min under nitrogen ambience was performed.

Devices were stored and characterized in a glove box under nitrogen ambient. All electrical characterizations were performed using Keithley 2636A. Transfer characteristics I_D-V_{GS} were plotted at room temperature. All the measurements were made in the same conditions, the gate-source voltage V_{GS} is varied from -20V to 60V with a 0.5V step, at constant drain-source voltage V_{DS} (+10 V or +100 V). The procedure allows to plot the transfer characteristics in linear and in saturation regimes.

Electrical parameters of both OFETs types in linear and saturation regimes have been summarized in Table I. As usual, equations for MOSFETs have been used in both regimes. The drain current I_D in linear regime ($V_{DS} << V_{GS}$-V_{TH}) is given by:

$$I_D = \frac{W}{L}\mu_{FE}C_{ins}(V_{GS} - V_{TH})V_{DS} \quad (1)$$

Where W and L are the width and length of the channel, μ_{FE} is the field-effect mobility, C_{ins} is the capacitance of the gate insulator per area unit and V_{TH} is the threshold voltage. The first derivative of I_D-V_{GS} curve at constant V_{DS} is the transconductance g_m given by:

$$g_m = \mu_{FE}\frac{WC_{ins}V_{DS}}{L} \quad (2)$$

The threshold voltage V_{TH} is the gate voltage axis intercept of I_D-V_{GS} curve plotted in linear representation. The field-effect mobility μ_{FE} is deduced from the extraction of g_m. The given value in Table I is the maximum value of μ_{FE}. The subthreshold swing SS has been extracted from I_D-V_{GS} curve plotted in semi-logarithmic scale using relation 3.

$$S = \left(\frac{\partial log(I_D)}{\partial V_{GS}}\right)^{-1}_{Max} \quad (3)$$

In the saturation regime ($V_{DS} >> V_{GS}$-V_{TH}), the drain current is given by:

$$I_D = \frac{W\mu_{FE}C_{ins}}{2L}(V_{GS} - V_{TH})^2 \quad (4)$$

In this case, the slope of the square root of I_D as a function of V_{GS}, $W\mu_{FE}C_{ins}/L$, will give the mobility μ_{sat} in saturation regime. The threshold voltage V_{TH} is the gate voltage axis intercept of $I_D^{1/2}$-V_{GS} curve.

CONFLICTS OF INTEREST

There are no conflicts to declare.

REFERENCES

1. H. Sirringhaus, *Adv. Mater.*, 2014, **26**, 1319-1335.
2. J. T. E. Quinn, J. Zhu, X. Li, J. Wang and Y. Li, *J. Mater. Chem. C*, 2017, **5**, 8654-8681.

3. X. Gao and Y. Hu, *J. Mater. Chem. C*, 2014, **2**, 3099-3117.
4. K. Zhou, H. Dong, H.-L. Zhang and W. Hu, *Phys. Chem. Chem. Phys.*, 2014, **16**, 22448-22457.
5. Y. Xu, C. Liu, D. Khim and Y.-Y. Noh, *Phys. Chem. Chem. Phys.*, 2015, **17**, 26553-26574
6. Y. Yuan, G. Giri, A. L. Ayzner, A. P. Zoombelt, S. C. B. Mannsfeld, J. Chen, D. Nordlund, M. F. Toney, J. Huang and Z. Bao, *Nat. Commun.*, 2014, **5**, 3005.
7. Z.-H. Wu, Z.-T. Huang, R.-X. Guo, C.-L. Sun, L.-C. Chen, B. Sun, Z.-F. Shi, X. Shao, H. Li and H.-L. Zhang, *Angew. Chem. Int. Ed.*, 2017, **56**, 13031-13035.
8. G. Schweicher, V. Lemaur, C. Niebel, C. Ruzié, Y. Diao, O. Goto, W. Y. Lee, Y. Kim, J. B. Arlin, J. Karpinska, A. R. Kennedy, S. R. Parkin, Y. Olivier, S. C. B. Mannsfeld, J. Cornil, Y. H. Geerts and Z. Bao, *Adv. Mater.*, 2015, **27**, 3066-3072.
9. J. Liu, H. Zhang, H. Dong, L. Meng, L. Jiang, L. Jiang, Y. Wang, J. Yu, Y. Sun, W. Hu and A. J. Heeger, *Nat. Commun.*, 2015, **6**, 10032.
10. F. R. Libsch and J. Kanicki, *Appl. Phys. Lett.*, 1993, **62**, 1286-1288.
11. T. Sekitani, S. Iba, Y. Kato, Y. Noguchi, T. Someya and T. Sakurai, *Appl. Phys. Lett.*, 2005, **87**, 073505.
12. D. K. Hwang, C. Fuentes-Hernandez, J. B. Kim, W. J. Potscavage and B. Kippelen, *Org. Electron.*, 2011, **12**, 1108-1113.
13. D. K. Hwang, K. Lee, J. H. Kim, S. Im, J. H. Park and E. Kim, *Appl. Phys. Lett.*, 2006, **89**, 093507.
14. C. Goldmann, D. J. Gundlach and B. Batlogg, *Appl. Phys. Lett.*, 2006, **88**, 063501.
15. H. L. Gomes, P. Stallinga, F. Dinelli, M. Murgia, F. Biscarini, D. M. de Leeuw, T. Muck, J. Geurts, L. W. Molenkamp and V. Wagner, *Appl. Phys. Lett.*, 2004, **84**, 3184-3186.
16. S. J. Zilker, C. Detcheverry, E. Cantatore and D. M. d. Leeuw, *Appl. Phys. Lett.*, 2001, **79**, 1124-1126.
17. J.-D. Peltier, B. Heinrich, B. Donnio, E. Jacques, J. Rault-Berthelot and C. Poriel, *ACS Appl. Mater. Interfaces*, 2017, **9**, 8219-8232.
18. S. Bebiche, I. Bouhadda, T. Mohammed-Brahim, N. Coulon, J. F. Bergamini, C. Poriel and E. Jacques, *Solid-State Electron.*, 2017, **130**, 49-56.
19. T. Umeda, D. Kumaki and S. Tokito, *Org. Electron.*, 2008, **9**, 545-549.
20. R. Häusermann and B. Batlogg, *Appl. Phys. Lett.*, 2011, **99**, 083303.
21. K. P. Pernstich, S. Haas, D. Oberhoff, C. Goldmann, D. J. Gundlach, B. Batlogg, A. N. Rashid and G. Schitter, *J. Appl. Phys.*, 2004, **96**, 6431-6438.
22. S. G. J. Mathijssen, M. J. Spijkman, A. M. Andringa, P. A. v. Hal, I. McCulloch, M. Kemerink, R. A. J. Janssen and D. M. d. Leeuw, *Adv. Mater.*, 2010, **22**, 5105-5109.
23. M. Romain, D. Tondelier, O. Jeannin, B. Geffroy, J. Rault-Berthelot and C. Poriel, *J. Mater. Chem. C*, 2015, **3**, 9701-97014.
24. M. Romain, S. Thiery, A. Shirinskaya, C. Declairieux, D. Tondelier, B. Geffroy, O. Jeannin, J. Rault-Berthelot, R. Métivier and C. Poriel, *Angew. Chem. Int. Ed.*, 2015, **54**, 1176-1180.
25. A. G. Fix, D. T. Chase and M. M. Haley, in *Top. Curr. Chem*, eds. J. S. Siegel and Y.-T. Wu, Springer, 2014, pp. 159-195.
26. M. Romain, D. Tondelier, B. Geffroy, O. Jeannin, E. Jacques, J. Rault-Berthelot and C. Poriel, *Chem. Eur. J.*, 2015, **21**, 9426–9439.
27. M. Romain, C. Quinton, D. Tondelier, B. Geffroy, O. Jeannin, J. Rault-Berthelot and C. Poriel, *J. Mater. Chem. C*, 2016, **4**, 1692-1703.
28. C. Poriel, R. Métivier, J. Rault-Berthelot, D. Thirion, F. Barrière and O. Jeannin, *Chem. Commun.*, 2011, **47**, 11703-11705.
29. L.-C. Chi, W.-Y. Hung, H.-C. Chiu and K.-T. Wong, *Chem. Commun.*, 2009, 3892-3894.

30. M. Romain, D. Tondelier, J.-C. Vanel, B. Geffroy, O. Jeannin, J. Rault-Berthelot, R. Métivier and C. Poriel, *Angew. Chem. Int. Ed.*, 2013, **52**, 14147-14151.
31. D. Thirion, M. Romain, J. Rault-Berthelot and C. Poriel, *J. Mater. Chem.*, 2012, **22**, 7149-7157.
32. C. Poriel, J. Rault-Berthelot and D. Thirion, *J. Org. Chem.*, 2013, **73**, 886-898.
33. C. Poriel, F. Barrière, D. Thirion and J. Rault-Berthelot, *Chem. Eur. J.*, 2009, **15**, 13304-13307.
34. F. Barrière, C. Poriel and J. Rault-Berthelot, *Electrochim. Acta*, 2013, **110**, 735-740.
35. K. H. Lee, S. O. Kim, J. N. You, S. Kang, J. Y. Lee, K. S. Yook, S. O. Jeon, J. Y. Lee and S. S. Yoon, *J. Mater. Chem.*, 2012, **22**, 5145-5154.
36. J. Kim, S. H. Kim, I. H. Jung, E. Jeong, Y. Xia, S. Cho, I.-W. Hwang, K. Lee, H. Suh, H.-K. Shim and H. Y. Woo, *J. Mater. Chem.*, 2010, **20**, 1577-1586.
37. S. Chaurasia, C.-J. Liang, Y.-S. Yen and J. T. Lin, *J. Mater. Chem. C*, 2015, **3**, 9765-9780.
38. H. Usta, A. Facchetti and T. J. Marks, *Acc. Chem. Res.*, 2011, **44**, 501-510.
39. H. Usta, C. Risko, Z. Wang, H. Huang, M. K. Deliomeroglu, A. Zhukhovitskiy, A. Facchetti and T. J. Marks, *J. Am. Chem. Soc.*, 2009, **131**, 5586-5608.
40. Y.-I. Park, J. S. Lee, B. J. Kim, B. Kim, J. Lee, D. H. Kim, S.-Y. Oh, J. H. Cho and J.-W. Park, *Chem. Mater.*, 2011, **23**, 4038-4044.
41. M. Romain, M. Chevrier, S. Bebiche, T. Mohammed-Brahim, J. Rault-Berthelot, E. Jacques and C. Poriel, *J. Mater. Chem. C*, 2015, **3**, 5742-5753.
42. Z. P. Fan, X. Y. Li, X. E. Luo, X. Fei, B. Sun, L. C. Chen, Z. F. Shi, C. L. Sun, X. Shao and H. L. Zhang, *Adv. Funct. Mater.*, 2017, **27**, 1702318.
43. T. Nakagawa, D. Kumaki, J.-I. Nishida, S. Tokito and Y. Yamashita, *Chem. Mater.*, 2008, **20**, 2615-2617.
44. M. Ozdemir, D. Choi, G. Kwon, Y. Zorlu, H. Kim, M.-G. Kim, S. Seo, U. Sen, M. Citir, C. Kim and H. Usta, *RSC Adv.*, 2016, **6**, 212-226.
45. Q. Meng and W. Hu, *Phys. Chem. Chem. Phys.*, 2012, **14**, 14152-14164.
46. E. Jacques, M. Romain, A. Yassin, S. Bebiche, M. Harnois, T. Mohammed-Brahim, J. Rault-Berthelot and C. Poriel, *J. Mater. Chem. C*, 2014, **2**, 3292-3302.
47. N. Cocherel, C. Poriel, J. Rault-Berthelot, F. Barrière, N. Audebrand, A. M. Z. Slawin and L. Vignau, *Chem. Eur. J.*, 2008, **14**, 11328-11342.
48. S. Thiery, D. Tondelier, B. Geffroy, O. Jeannin, J. Rault-Berthelot and C. Poriel, *Chem. Eur. J.*, 2016, **22**, 10136-10149.
49. C. Poriel, N. Cocherel, J. Rault-Berthelot, L. Vignau and O. Jeannin, *Chem. Eur. J.*, 2011, **17**, 12631-12645.
50. C. B. Nielsen, E. Voroshazi, S. Holliday, K. Cnops, B. P. Rand and I. Mc Culloch *J. Mater. Chem. A*, 2013, **1**, 73-76.
51. A. P. Kulkarni, C. J. Tonzola, A. Babel and S. A. Jenekhe, *Chem. Mater.*, 2004, **16**, 4556-4573.
52. C. M. Cardona, W. Li, A. E. Kaifer, D. Stockdale and G. C. Bazan, *Adv. Mater.*, 2011, **23**, 2367-2371.
53. J. Rault-Berthelot, C. Poriel, F. Justaud and F. Barrière, *New J. Chem.*, 2008, **32**, 1259-1266.
54. W. B. Jackson, J. M. Marshall and M. D. Moyer, *Phys. Rev. B J1 - PRB*, 1989, **39**, 1164-1179.
55. M. J. Powell, *Appl. Phys. Lett.*, 1983, **43**, 597-599.
56. R. V. Chamberlin, *J. Appl. Phys.*, 1985, **57**, 3377-3381.
57. P. Grassberger and I. Procaccia, *J. Chem. Phys*, 1982, **77**, 6281-6284.
58. R. Meaudre, M. Meaudre, P. Jensen and G. Guiraud, *Philos. Mag. Lett.*, 1988, **57**, 315-320.
59. K. O. Jeppson and C. M. Svensson, *J. Appl. Phys.*, 1977, **48**, 2004-2014.
60. M. J. Powell, C. v. Berkel and J. R. Hughes, *Appl. Phys. Lett.*, 1989, **54**, 1323-1325.
61. S. G.J. Mathijssen, M. Cölle, H. Gomes, E. Smits, B. de Boer, I. McCulloch, P. Bobbert and D. Leeuw, *Adv. Mater.*, 2007, **19**, 2785-2789.

62. R. Ahmed, C. Simbrunner, G. Schwabegger, M. A. Baig and H. Sitter, *Org. Electron.*, 2014, **15**, 3203-3210.
63. R. Ahmed, A. Kadashchuk, C. Simbrunner, G. Schwabegger, M. A. Baig and H. Sitter, *ACS Appl. Mater. Interfaces*, 2014, **6**, 15148-15153.
64. R. Ahmed, C. Simbrunner, M. A. Baig and H. Sitter, *ACS Appl. Mater. Interfaces*, 2015, **7**, 22380-22384.